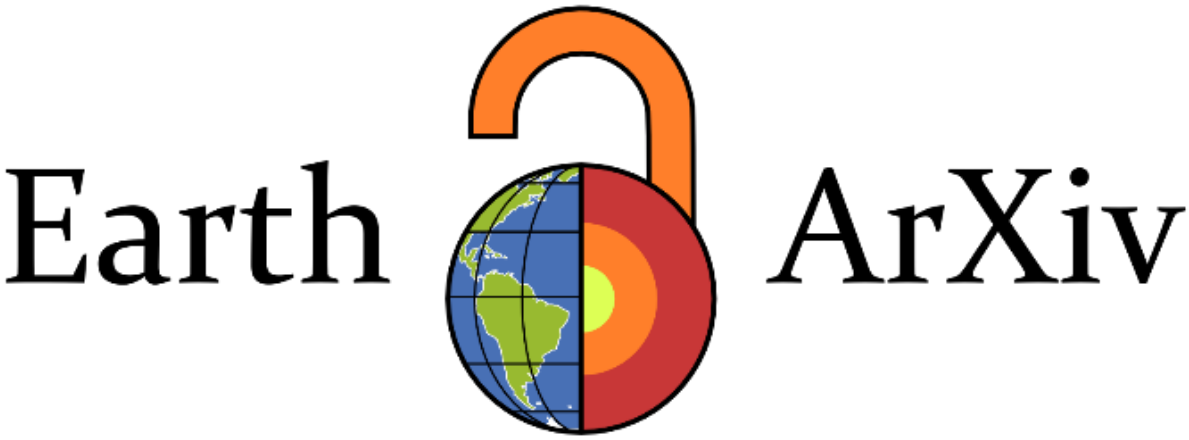

Prediction of Land Surface Temperature under overcast skies using Data Fusion and Deep Learning approach

Dhwanilnath Gharekhan[a]*

[a]Independent Author
*Corresponding Author: dhwanilnath@gmail.com

Abstract

Land Surface Temperature (T_s) is an essential input to drive surface energy balance for modelling terrestrial ecosystem processes. It serves as a vital indicator of drought, global change, urban heat islands, public health, and most importantly to understand monsoonal water stress signatures. Thermal InfraRed (TIR) remote sensing is the only source to retrieve T_s. Retrieval of T_s in the tropics and sub-tropics is regularly hindered due to persistent overcast skies during monsoon, limiting the seamless T_s data availability. Present study demonstrates the potential of Artificial Neural Network (ANN) to predict T_s over Indian landmass in overcast conditions using a three-stage multisource data-fusion approach. The L_{out} flux was predicted in the first stage using two five-layer deep learning-based ANN algorithms between 2015-2020. The trained ANN models provided a correlation (r) of 0.99 for daytime and 0.97 for night-time with Root Mean Square Error (RMSE) within 2%. The models' outputs were upscaled to a spatial resolution of 4 km and compared with NCEP reanalysis fluxes (day and night-time algorithms combined) producing r = 0.83 and RMSE of 10%. Furthermore, T_s was retrieved using MODIS and other products and compared with ECMWF Reanalysis v5 (ERA5). The predicted LST provided a strong correlation (r = 0.98) with in-situ measurements leading to mean absolute error (MAE) of 2.4 K.

Keywords: Land Surface Temperature, Thermal Infrared, Outgoing Longwave Radiation, Artificial Neural Network, INSAT3D

1. Introduction

Land Surface Temperature (T_s) is a key parameters within the land surface interaction, It plays an essential role within the energy exchange on a regional and global scale with implications and influences of urban heat island studies, global warming etc. [1]. The current T_s products are derived through the thermal infrared bands within remotely sensed imaged at a high temporal and continuous observation. Finer resolution observations are also used within several studies. [2]. However, due to the strong variability within the surface feature and parameters like soil moisture, land cover types, the images are strongly affected and it leads to challenges in effectively capturing T_s over different time periods. Furthermore, the resolutions are very course in nature, to compensate with the temporal resolution [3]. This can lead to lot of hinderances within the T_s centric retrieval and application studies. The contaminations are also strongly influenced within the vertical column of a pixel space, when observed through the atmosphere. The incorporation of atmospheric contamination like clouds and other overcast conditions, restricts the capabilities of sensors to retrieve these T_s measurements. This leads to missing measurements and pixels. Due which T_s retrieval from outgoing longwave radiation (LW_{out}) is a standard approach in thermal remote sensing [4].

Over the vertical column, LW_{out} is governed by the interactions of atmospheric absorption and emission [[5], [6]]. Culf and Gash (1993) provided an observation conclusion that during a standard atmosphere within a dry season, there is a reduction in the lapse rate, however, there is a high lapse rate with strong water vapor-based humidity presence. This entails the variability of R_l in a sinusoidal pattern especially in tropical regions with high seasonal variability [7], [8]]. The emissivity and temperature are the key influencers for the variations in R_l. R_l is also influenced by local parameters like soil, vegetation cover (or vegetation fraction – VF), land use type, the structure and spread of vegetation, the surrounding influences of high trees or buildings, and

water vapour (Relative humidity – RH and vertical precipitable water – TPW), cloud cover, Earth's skin temperature, air temperature (T_a), surface emissivity, T_s etc. [[9], [10]]. Earth's average temperature is very stable due to balance of incoming and outgoing radiation [11]. Under cloudless skies, the estimates are directly driven by the emissivity and temperature. The presence of overcast conditions (like cloud and fog) can directly influence the longwave radiation budget in different ways [12]. The influence of the overcast conditions, which can lead to change in the Earth energy for incoming solar radiation and outgoing thermal infrared radiation is termed as Cloud or Fog Radiative Forcing (RF). This depends on (i) the present atmospheric concentration of the clouds / fog (ii) wavelength at which the molecules absorb (iii) the absorbing rate per molecule [13]. An overcast correction factor 'c' has been introduced by Crawford & Duchon (1999), which can account for these effects on radiation fluxes:

$$c = 1 - \frac{SW_{in}}{R_{ext}} \quad (1)$$

Where R_{ext} is Extra-terrestrial solar radiation (at the top of the atmosphere) (Wm^{-2}). The Overcast fraction is a direct indication of the RF generated by clouds or fog, which influences the longwave radiation. Greater the fraction or the temperature difference between the surface and cloud/fog top, higher is the longwave overcast RF [14]. The RF driven by temperature is in direct relation with the longwave radiation while the RF by water vapor with high temperature tends to increase longwave radiation and reduces when temperature (T_a and T_s) and water vapor are low [[13], [15]]. Wild et al (2019) identified that under clear and overcast sky conditions the surface estimates were found to vary significantly [16]. Aerosols which are anthropogenic in nature, tend to impact the vertical column distribution, planetary albedo and clouds. The cloud-aerosol or fog-aerosol interaction leads to variations in longwave radiation [17]. The formula to derive LW_{out} is depicted in Eq. 2.

$$LW_{out} = \varepsilon_s \sigma T_s^4 \quad (2)$$

Where ε_s is the surface emissivity when compared to a black body in idea conditions, σ is Stephen Boltzmann's constant [5.67E-8 $K^{-4}Wm^{-2}$]. While the estimations can provide strong temporal studies, the challenges lie in the lack of availability of such datasets [18]. R_l (and its sub fluxes) is measured using pyrgeometers or all-weather observatories. The developing countries having tropical/subtropical climate have only few or no measurements [19]. While LW_{out} can be simulated using Radiative Transfer (RT) models such as SBDART or MODTRAN, the input data of specific parameters like water vapour, CO_2, aerosol, cloud and surface data are not typically available under all-sky conditions diurnally, especially in tropical and subtropical climate [[20], [21]].Over the years, several site-specific models were developed to compensate the limitation and scarcity of measuring instruments [[20], [22], [23]]. Very limited number of site-specific models are available which need to be locally calibrated for usage. The restrictive meteorological conditions associated with the site-specific models tend to increase error significantly [24]. The linear (or multivariate – MVR) models can estimate LW_{out} over specific conditions, however multisource multisite datasets require better computations and more precise models. While these meteorological parameters (Ta, RH, c, TPW, COT, VF) can be sufficient for estimating LW_{out} under overcast-sky conditions over varied agro-climatic settings, the elevation (Z) variability was found to be a vital driving factor keeping in view of multi-source and multi-location applicability. As the elevation alters, the vertical column width and lapse rate get altered as well [25]. However, the surface information regarding earth's skin temperature can be missing under cloudy skies. The lack of measurements especially during nocturnal time period are required for the estimation of LW_{out} properly. Microwave measurement which provides atmospheric and surface parameters like surface temperature is considered an alternative as microwave penetrates through the atmosphere irrespective of the composition [26]. Brightness temperature (BT) is the temperature of a blackbody that would emit the same amount of radiation as the targeted body in a specified spectral band can be used as an alternative for estimating LW_{out} in the absence of T_s measurements [27].

With the current development of high computation tools at researchers' disposal, several studies are attempting to resolve the multi-sourced multiple conditions studies. This is specifically useful, since generalised empirical equations becomes a hindrance. Machine learning and Artificial Neural Networks (ANN) became an alternative that could (i) handle high magnitudes of datasets, (ii) devise multisource and multilocation datasets, (iii) outperformed linear models with fixed region or location-specific coefficients [28]. There is a need to explore non-linear interactions of influencing factors and Artificial Neural Network (ANN) techniques to estimate LW_{out} especially under cloudy skies over diverse agro-climatic settings in sub-tropical and tropical climate. The current study aims (i) to develop new multi-variate and ANN-based deep learning (DL) models for LW_{out} estimation

under overcast sky conditions using multi-location data over the Indian sub-tropical landmass, (ii) To compare the performance of the newly developed ANN-based DL model for day time conditions, separately (iii) To derive T_s under overcast sky conditions using the newly developed DL model.

2. Study Region

The study was carried out using the R_l measurements on LW_{in} and LW_{out} components from net radiometers mounted at 2m height on a flux tower. The net radiometers were installed along with eddy covariance system under the Indo-UK INCOMPASS (INteraction of Convective Organization and Monsoon Precipitation, Atmospheric Surface and Sea) project [[29], [30]]. In the flux tower measurement system, a net radiometer (Kipps and Zonen CNR4) is installed along with meteorological assembly. This is a four-component net radiometer that measures SW_{in}, SW_{out}, LW_{in} and LW_{out} fluxes with an uncertainty in daily total of less than 10% (at 95% confidence level) [31] [32]. The component has a high response time with less than 18 seconds, with a sensitivity measurement ranging from 5 to 20 $\mu V\ W^{-1}\ m^2$. The meteorological assembly measures relative humidity and air temperature with an uncertainty in daily values of less than 15% (at 95% confidence level) [[31], [32]]. Under INCOMPASS, eight locations were identified for their diverse terrestrial eco-systems [33], out of which 5 locations were chosen for this study for their unique agro-climatic settings and having continuous LW_{in} and LW_{out} data records. The details of land use conditions and climate type of the study sites are mentioned below:

Table 1 : Study site characteristics where net radiometers and meteorological assembly were installed under INCOMPASS programme along with Eddy flux system

Sr. no.	In-situ observational station	State	Geographical Coordinates		Height (meters)	Land cover	Climate
			Lat (°) (N)	Long (°) (E)			
1.	Chandan, Jaisalmer (JAI)	Rajasthan	26.99	71.34	196	Grassland	Arid
2.	UAS, Dharwad (DHA)	Karnataka	15.50	74.99	656	Crop land	Semi-Arid
3.	Indian Institute of Technology-K, Kanpur (KAN)	Uttar Pradesh	26.51	80.22	128	Grassland	Humid
4.	Nawagam, Kheda (KHE)	Gujarat	22.80	72.57	55	Crop land	Semi-Arid
5.	Pusa, Samastipur (SAM)	Bihar	26.00	85.67	39	Crop land	Humid

3. Data Used

3.1 In situ measurements

The study used measurements of LW_{out} and associated meteorological variables (T_a and RH) in July to February during 2015 to 2018 which is influenced by the south-west monsoon clouds between July-Oct and by radiative fog during November to February in the winter season. The measurements for the above period were used for ML model training and testing. and the validation was carried out on spatial scale during 2019 and 2020. The sensors measure at high temporal intervals of 10 seconds. The measurements were resampled and averaged over 30 minutes' time interval and were segregated into 70:30 ratio [34] for training (9735 points) and validation (4173 points) datasets.

3.2 Satellite Based Products

Satellite datasets provide large volume of measurements for specific parameters on a high temporal time period [35]. The details of satellite-based input variables are given in the Table 2 and 3.

Table 2: Satellite-based atmospheric products used in this study to predict and compare LW_{out} and T_s under cloudy conditions

Sr. no.	Input variables	Unit	Spatial resolution	Satellites	Data code	Temporal resolution	Source link
1.	SW_{in}	Wm^{-2}	0.05º	INSAT 3D	3DIMG_INS	30 minutes	https://mosdac.gov.in/
2.	Z	m	0.01º	SRTM	SRTM_1km	-	ftp://e0srp01u.ecs.nasa.gov/srtm/version2/SRTM3/
3.	BT	K	0.25 º	SCATSAT 1	SCATSAT_BTH_IND	Daily	https://mosdac.gov.in/
4.	VF	-	0.01º	SPOT-VGT	FCOVER	10 days	https://land.copernicus.eu/global/products/fcover
5	ε_s	-	0.05º	MODIS Aqua	MYD11C3	Monthly	https://ladsweb.modaps.eosdis.nasa.gov/search/

Table 3: Other gridded-meteorological products used in this study to estimate and compare LW_{out} and T_s under cloudy conditions

Sr. no.	Input variables	Unit	Spatial resolution	Satellites	Data code	Temporal resolution	Source link
1.	T_a	K	0.05°	WRF	t2	3 hours	https://mosdac.gov.in/
2.	RH	%	0.05°	WRF	rh	3 hours	https://mosdac.gov.in/
3.	ERA_LST	K	0.1º	ERA5 Reanalysis	LST	Hourly	https://www.ecmwf.int/en/forecasts/dataset/ecmwf-reanalysis-v5
4.	TPW		0.25º	NCEP Reanalysis II	TPW	6 hourly	https://www.cpc.ncep.noaa.gov/products/wesley/reanalysis2/
5.	NCEP_LW_{out}	Wm^{-2}	0.25º	NCEP Reanalysis II	LW_{out}	4 hourly	https://www.cpc.ncep.noaa.gov/products/wesley/reanalysis2/

Cloud fraction 'c' was derived using the equation mentioned in Equation 4, with a temporal resolution matching to SW_{in} and R_{ext} was derived using a set of astronomical formulae for a given location coordinates, time and day of the year. The TPW represents the vertical total water vapor presence between the earth surface and top-of-atmosphere [[36], [37], [38]]. The product has a temporal resolution of 6 hours and for this study the TPW within 6 hours was considered static. SRTM (Shuttle Radar Topography Mission) is a radar mission launched by NASA with the mission of mapping 80% of the earth surface in a single 10-day space shuttle flight. It produced digital elevation datasets with spatial resolution of 30m between 60°N and 54°S latitude using Synthetic Aperture Radar (SAR) interferometry using C-band [39]. Vegetation fraction is a normalised range defining the concentration of vegetation cover within a pixel, SPOT-VGT hosted by the Copernicus land service programme [[40], [41]] provides vegetation parameters with a spatial resolution 1 km and 300m with a temporal resolution of 10 days. The 1km product was considered due to the need for rescaling them to the LST resolution of 0.05 º. Brightness temperature is measured by SCATSAT 1 which carries a Ku band sensors obtaining the surface temperature over a land surface with a temporal resolution of 1 day [[42], [43]].

4. Methodology

4.1 Data Fusion Approach

Multisource datasets-based models can be achieved using data fusion technique. These techniques provide a better understanding of the targeted variable using linear and nonlinear relationships. LEO (Low Earth Orbiting) satellites, which can produce coarse temporal observations (up to 4 like MODIS TERRA AND AQUA) during a 24hour cycle at a good spatial resolution and GEO (Geostationary Earth Orbiting), which can provide high temporal observations of 30minutes, but at coarser resolutions of 5 to 10kms [[44], [45],[46],[47]]. A combined approach can harness the capabilities of both types of satellite observations and also enhance their shortcomings to provide strong and vital insights into the different studies, they are being used in, like LW_{out} variabilities. Furthermore, with multiple parameters, a focus approach can be built on [48]. While data fusions techniques operate for estimations be derived for spatial scales, the estimates to be used for empirical estimates can be troublesome especially for MVR models.

LW_{out} (clear) can be directly quantified through Eq. 2. Where ε_s will be acquired from MODIS TERRA and AQUA, the T_s will be taken from the already operationalized INSAT 3D product. Thus, the quantisation will be defined as:

$$LW_{out} = \mathrm{f}(LW_{out\_clr}, LW_{out\_overcast}) \tag{3}$$

$$LW_{out} = f[(\varepsilon_{s\_clr}\sigma T_{s\_clr}^4), f(BT, TPW, VF, RH, T_a, SW_{in})] \tag{4}$$

Here, the Eq. 3, highlights the combination of gap filling approach, under all sky conditions. Where the second part of the function cannot be estimated empirically, the estimates such as T_s whose measurements cannot be acquired due to cloud presence cannot be derived using MVR models. Lack of surface parameters like T_s can restrict the understanding of the surface. Combining Data Fusion approach along with machine learning techniques can provide a substantial gap bridge for in parameter estimations. The resultant quantization will be become of function of different parameters and the cloudy pixels will be gap filled using the model developed among multisource datasets.

4.2 Machine Learning model architecture for LWout prediction

"An Artificial Neural Network (ANN) is a computational model that is inspired by the way biological neural networks in the human brain process information" [49]. As mentioned earlier, ANNs are the most widely acceptable approach within the temperature and solar radiation-based studies [28]. However, when dealing with second derivative approach, where another parameter is derived using the estimated output of an ANN based approach; deep networks until 5 layers is needed [50]. Alternatively approach like Back-propagation and Levenberg Marquardt (LM) approach, which improve the performance of the models by reducing the error through the combination of the Gauss-Newton algorithm (speed) and the steepest gradient decent method (stability) [51] cab provide a strong solution and reduce computation strain on the systems [52], [53] through the activation function and Jacobin Matrix.

The activation function projects the non-linearity into the input, based on the mathematical function defined [54], like sigmoid function. The approach uses a normalisation operation, with a threshold and are considered highly for meteorological and radiation based studies [[55]; [56]; [57]; [34]; [58], [59]]. The current approach incorporates these proofs and adapts a LM based function with a sigmoid activation to develop observations of LW_{out} under overcast-sky conditions. The flow diagram of DL model is given in Figure 1.

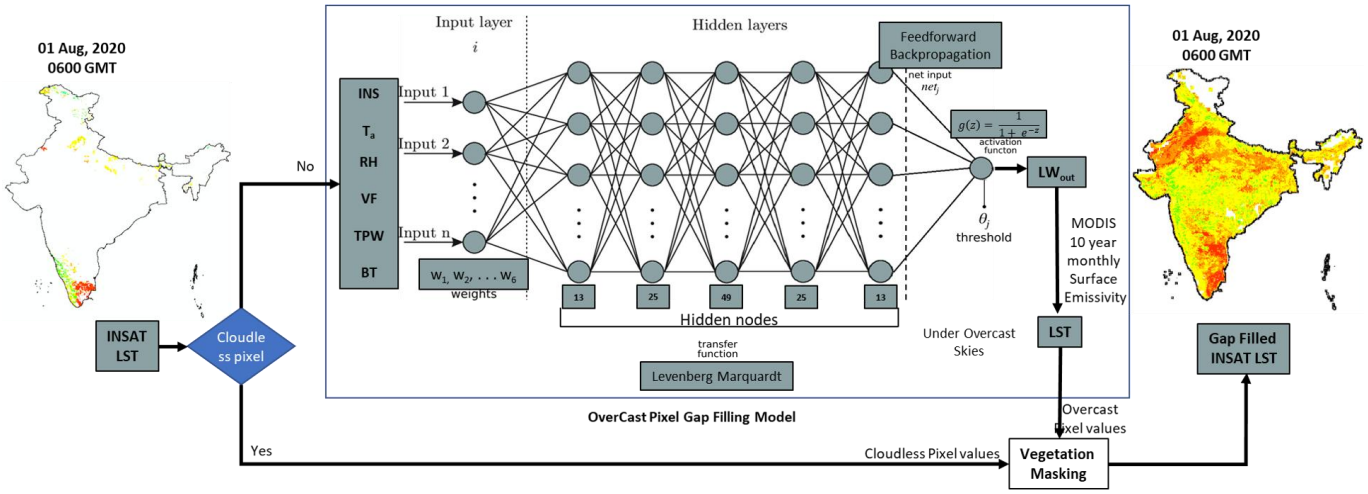

Figure 1. DL developed for estimation of LWout under overcast skies

The model was trained with 1000 iterations, while the condition was kept for the model to stop training provided it reaches the global minima of error, prior to the completion of iterations. The network was built using a sigmoid function as an activation, to get the desired performance. Within each single layer the number of neurons is based on a few rules. The study adapts the standard condition provided by Heaton, which follows the 2n – 1 rule, where n is the number of inputs from the previous layer. Along with the same, the symmetry between each side of the middle-hidden layer has been kept the same for better approximation [60]. With 7 inputs, the maximum number of hidden nodes i.e., 13, 25, 39, 25, 13 were considered for the 5 hidden layers. The performance was estimated using the Mean Square Error (MSE) and was identified at iteration number 291 with gradient being 132 (ranging between 1.51E6 and 1E-7) and μ of 0.1 after a 6-validation check for daytime within the number of iterations.

The model post training, filters the pixels based on the missing values. The existing pixels are filtered using a vegetation VF mask. The filtering is done to avoid errored computations within snow covered regions, as the model does not account for training sites from such regions. The missing pixels are computed within the DL model, where the inputs are acquired and the LW_{out} is derived. The T_s is derived from this LW_{out}, based on the Equation 5. The ε_s is compiled using 10 year monthly averaged MODIS dataset, where each month has been averaged over 10 years' dataset. This is done to gap fill missing value and remove anomalies. The derived T_s is used to gap fill the missing pixel values within the INSAT 3D LST product and provide a complete LST product. The above image gives an example of 01 August, 2020 at 6 Hrs GMT (-5.30 IST). The results for the same are discussed in Section 5.

4.3 Model sensitivity

The model, like any other are prone to sensitive undulations due to variations within the input parameters. Identifying the capability and the range of variations due each input towards the derived parameter is vital. The quantification can be done using a One-dimensional (1D) is a linear approach. The approach operates on the mean of each input level, while varying it through a specified range and their influence on the derived output (depicted in Figure 2) [61]. Along with the sensitivity, the correlation matrix of influences between the parameters has also been depicted.

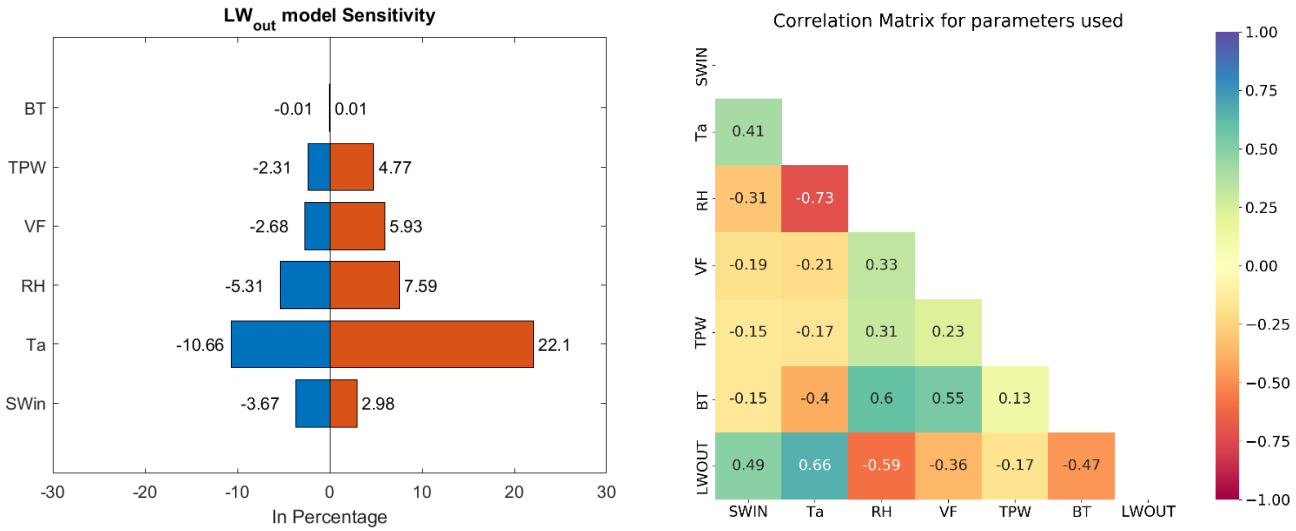

(a) (b)

Figure 2. Sensitivity Analysis (a) of the model developed and the Correlation Matrix (b) of the input features and output label

The sensitivity analysis depicted a very weak influence (±0.01) of BT with LW_{out} while changing the temperature by 3K, despite having a low negative correlation influence (-0.47). A similar trend was observed with SW_{in}, where despite having a decent influence of 0.49, the ±5% variation, only led to a 3% average variation in LW_{out}. The change in TPW and VF of the order of ±5% led to an average of 3% deviation in LW_{out}, which is corroborated with the low influence in the correlation matrix (TPW is -0.17 and VF is -0.36). The strongest influence was observed with T_a, having the highest positive correlation of 0.66, the model was highly sensitive towards LW_{out}. A ±5 K change let to an average variation of 17% in LW_{out}.

4.4 Retrieval of LST from predicted LW_{out}

The predicted LW_{out} from machine learning model is composed of outgoing longwave fluxes from land surfaces ($LW_{out(s)}$) and reflected component of incoming longwave radiation fluxes. Therefore, LW_{out} can be expressed as given in Eq. 5 and 6, after applying Kirchhoff's law,

$$LW_{out} = LW_{out(s)} + (1-\varepsilon_s)(LW_{in}) \quad (5)$$

$$LW_{out} = \sigma \varepsilon_s T_s^4 + (1-\varepsilon_s)(LW_{in}) \quad (6)$$

The prediction model of LW_{in} in cloudy and foggy sky conditions has already been developed using MLP-based ANN models ([62]; [63]). Land cover-based surface emissivity (ε_s) data from MODIS [MOD11C3] [64], MLP-model predicted LW_{in} and predicted LW_{out} from DL-model in the current study were used in the Eq. 5 and 6 to retrieve T_s in overcast skies.

4.5 Validation Strategies

Multiple combinations of ANN-based models were developed to identify the best fit combination for the LW_{out} estimates. The details of the combination have been explained in Section 0. With the best combination, the LW_{out} were estimated and compared with in-situ measurements. With good performance, the same model was used to derive spatial estimates of the same, at a 5km grid and compared with existing NCEP reanalysis product. The details have been mentioned in Section 0. The performance permitted the usage the spatial estimates in deriving T_s using MODIS derived surface emissivity and Eq. (1). The results, diurnal statistics and comparison have been exemplified in Section 0.

5. Results and Discussion

5.1 Comparison of ML models for LW_{out} prediction in overcast skies

The DL model developed in this study was computed over several iterations with the final model having 5 layers and uses 7 parameters (SW_{in}, T_a, RH, VF, TPW, BT) to estimate the LW_{out} under overcast conditions. Collectively, there are 11 combinations, their performance has been depicted in Table 3 and 4.

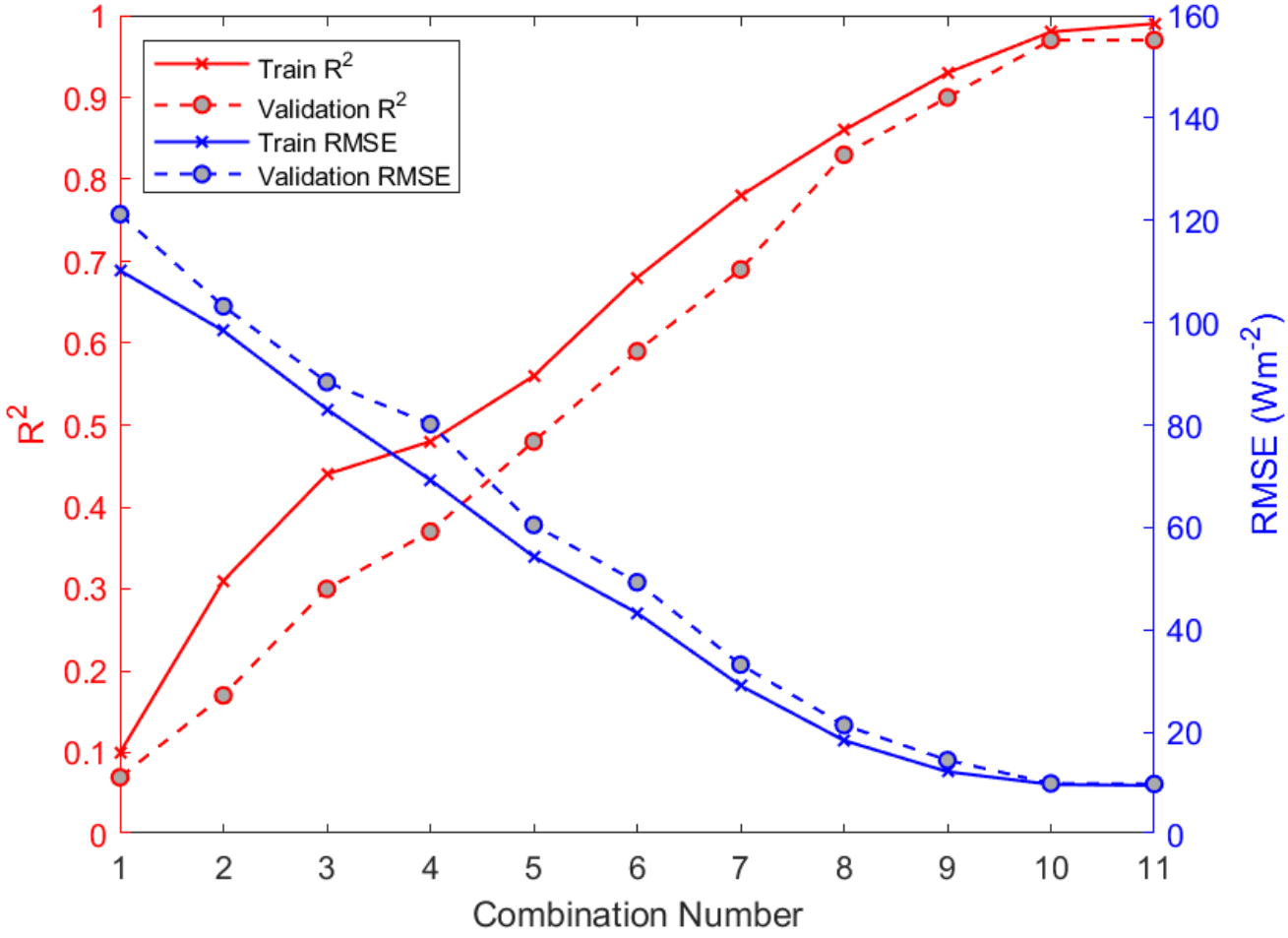

Figure 3. Performance of all machine learning and deep learning models considered and built for the study. The right axis depicts the RMSE and the left axis depicts the R^2 of each model.

Table 4. Performance of all machine learning and deep learning models considered and built for the study

Combination No.	Hidden Layers	No of parameters	Training		Validation	
			RMSE (Wm^{-2})	R^2	RMSE (Wm^{-2})	R^2
1	1	2	110.2	0.10	121.2	0.07
2	1	3	98.4	0.31	103.2	0.17
3	1	4	83.1	0.44	88.4	0.30
4	1	5	69.3	0.48	80.2	0.37
5	1	6	54.3	0.56	60.5	0.48
6	1	7	43.3	0.68	49.3	0.59
7	2	7	29.1	0.78	33.2	0.69
8	3	7	18.4	0.86	21.4	0.83
9	4	7	12.3	0.93	14.5	0.90
10	5	7	9.8	0.98	10.0	0.97
11	6	7	9.6	0.99	9.90	0.97

The model building was initially dependent on the number of parameters as input for a single hidden layer and furthermore, up till 6 hidden layers have been considered for the performance. However, the 6 layer – 7 parameter combination was not considered, because they model has started to saturate and would have overfit (as visible from Figure 3), if a new dataset was added. Considering the same, 5 layer – 7 parameter combination was eventually selected. The training and validation plots along with the collective histogram for the same are shown in Figure 4 and the corresponding performance statistics are mentioned in Table 5.

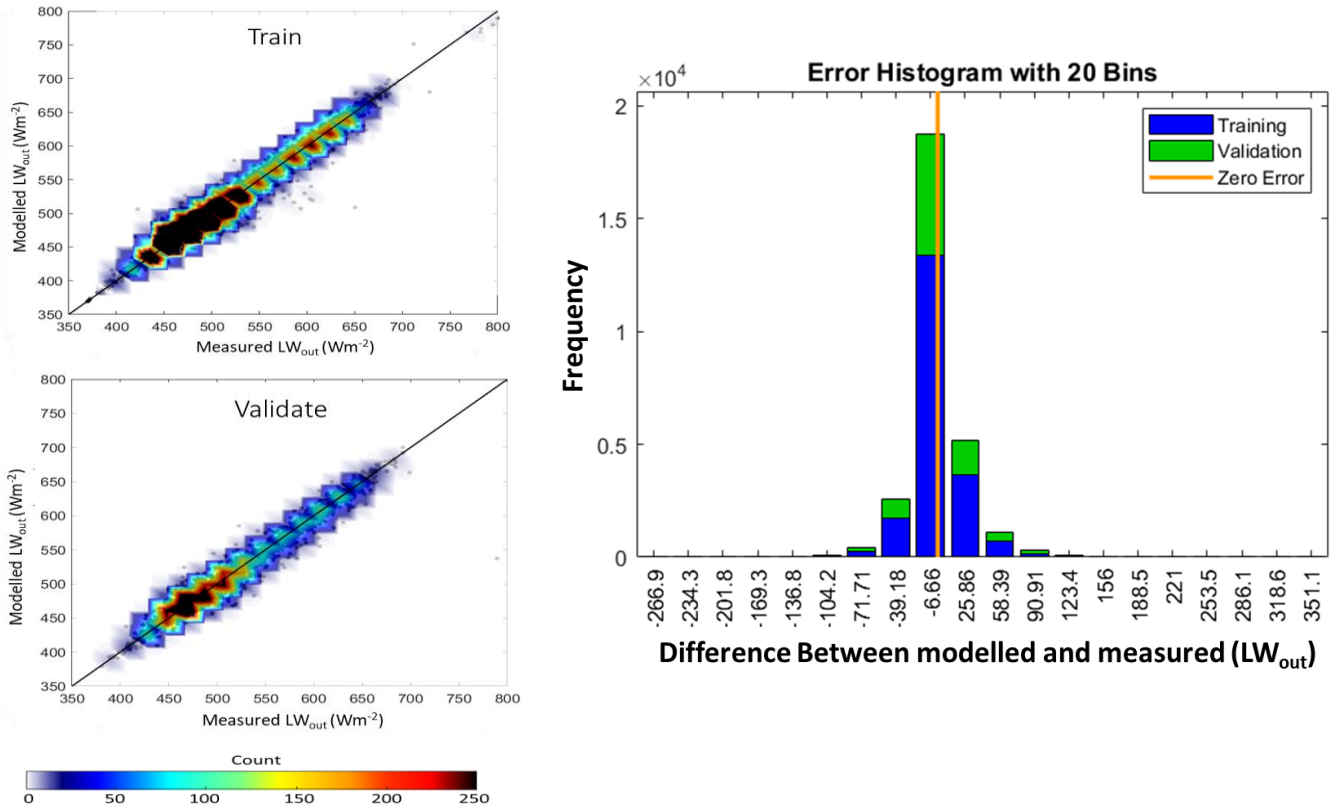

Figure 4. Scatter density plots of training (Top Left) and Validation (Bottom left) between best fit DL model estimates and insitu measurements; Error (measured – modelled LW_{out}) histogram (Right) between training and validation stages.

Table 5. Performance Statistics of DL model under overcast conditions

Model Stage	N	RMSE (Wm^{-2})	PRMSE (%)	MAE (%)	R^2
Training	9735	9.8	1.9	2.6	0.98
Validation	4173	10	2	2.6	0.97

The training and validation stage provided a good agreement between the modelled outputs and insitu measurements. The models although trained under selective sites, can be ported to different sites for prediction, provided they have similar agro-climatic settings as that of the Indian sub-tropics. The goal is to upscale the models for predictive purpose over a spatial scale, covering the Indian landmass.

5.1.1. Diurnal evaluation LW_{out} estimates

The diurnal estimates of LW_{out} during daytime from ML model in cloudy skies were compared with *in situ* measured LW_{out} at five different flux tower sites during 2015 to 2018. The datasets are spread across different time periods from the validation datasets. Since the original data was split randomly, the dates with continuous measurements have been depicted below. The comparison plots are shown in Figure 5.

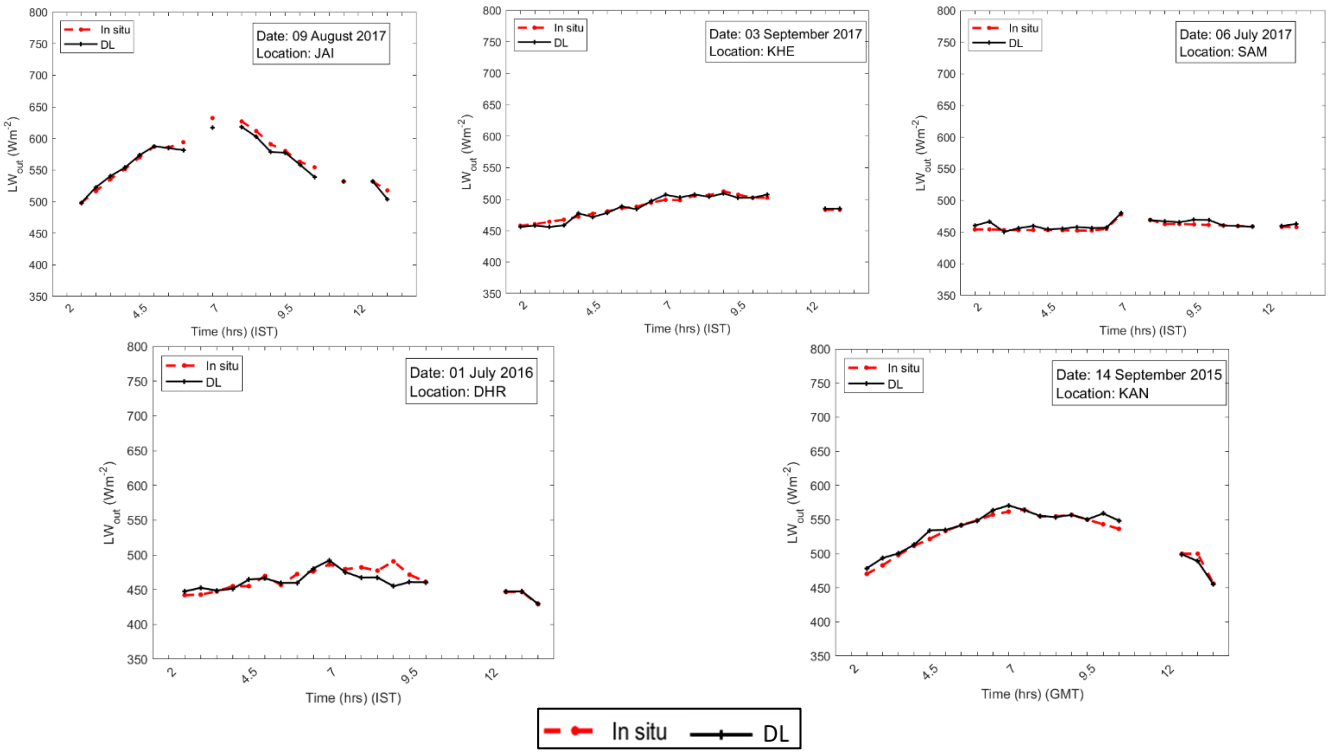

Figure 5. Diurnal Trends of LW_{out} over selective dates at different sites between model and in situ. The x-axis depicts time in GMT and y-axis depicts LW_{out} (in Wm^{-2}).

The graphs exemplify the diurnal trend variations between in-situ and model derived LW_{out}. The trends were closely matching between the two in most regions. The model has small undulation when comparing with the in-situ measurements. Like in JAI, the model was overperforming by a factor 5 Wm^{-2}. Whereas, in KAN, KHE and SAM, more undulations are necessarily observed in specific time periods like around 8-9.5 Hrs. The missing values between 10 to 12 Hrs are due to the lack of measurements within the in-situ measurements and a few satellite products within the model.

5.1.2 Spatial Estimates of LW_{out}

The point scaled DL model was upscaled to match with the INSAT 3D LST input of 5km grid. The model was used to compute spatial scale imageries, over the years of 2019-2020 during the overcast months. The resultant imageries for 0600 GMT time period are depicted in Figure 6.

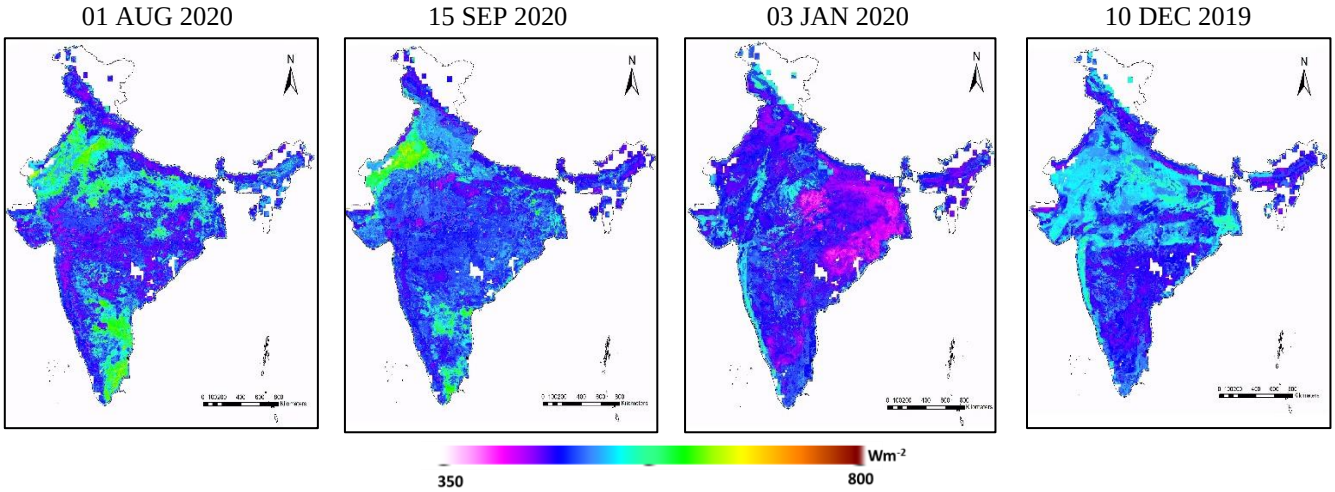

Figure 6. LW_{out} spatial output over the span of 4 months for the years 2019-2020 at 0600 GMT

The regional distribution of satellite-based LW_{out} estimates over Indian landmass at 0600 GMT on selected dates during 2019-2020 are exemplified above. The blank regions symbolize none agricultural regions, which were filtered out during the computational phase. The reason to avoid is to not provide inaccurate estimates, especially in regions with no vegetation like snow covered in the northern region of India. The change in colours when shifting from August to January, depict the change in seasons i.e., from south eastern monsoon to winter season. The low estimates, especially in the central north region i.e., near the Himalayan plateau, can be attributed to the shift in the overcast patterns i.e., clouds and fogs.

The spatial estimates were compared with the NCEP Reanalysis LW_{out} product. The resulting differences are depicted in Figure 7.

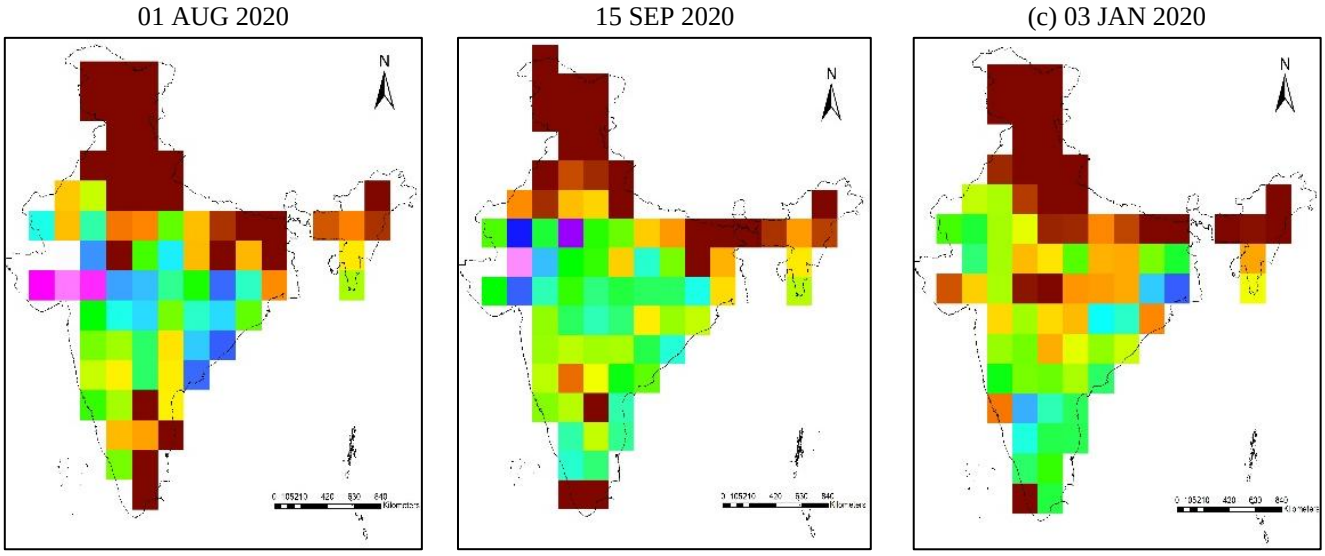

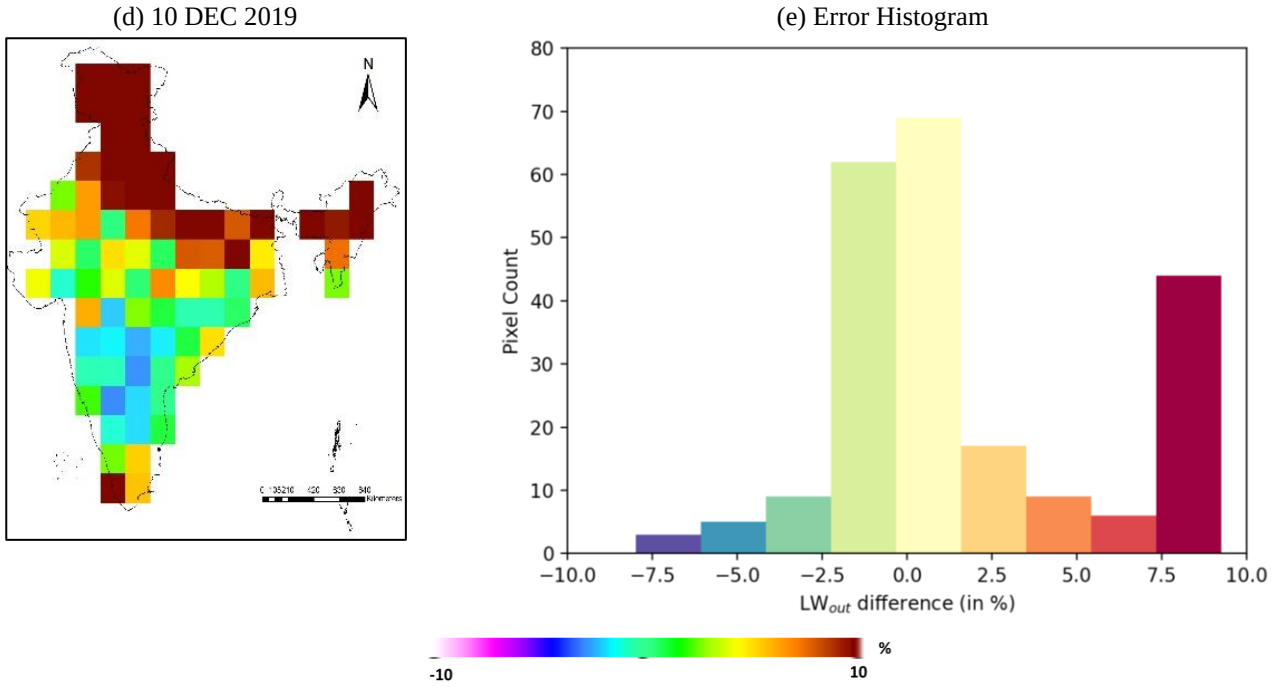

Figure 7. Difference between NCEP Reanalysis and model derived LW_{out} over selective days (a – 01 Aug 2020, b – 15 Sep 2020, c – 03 Jan 2020, d – 10 Dec 2019) for the year 2019-2020 at 0600 GMT and their collective (e) Error Histogram

The NCEP product provides the LW_{out} parameter at a 25km grid. The DL derived LW_{out} was resampled to match with the NCEP product resolution. Due which there was a lot of averaging within the estimates and with differences, more variations were observed. This is especially noted in the north Himalayan belt, where due to the valley and high elevation undulations. The estimated have been averaged out to a large extend, which leads to higher differences (of the scale of 9.7%) compared to the rest of India, where the average variations lied between -5 to 5%. These errors tend to increase significantly, especially near the boundary regions in specific sites, like in August, near the bottom. Even distributions in the central region were observed, well within the ±5% range. A distinctive variation was observed in the month of August in the western zone of Gujarat, the negative error was attributed to the low pressures being developed from the south western monsoon induced wind stress [[65], [66], [67]] and averaged upscale DL model measurements. The Error histogram (Fig 7.e) highlighted the regions where maximum variations is being observed. It can be noted that the maximum error lies between -4 to 4 %, of the error curve. While there is significant pixels with a 10 % error, but this has been attributed of it being on the boundaries, with more missing values (due vegetation mask). The errors will be reduced if in the future, more regions are incorporated within the model training, which can cover the non-vegetative regions as well.

5.2 T_S Prediction

The T_s was retrieved using Eq. 5 and 6 and procedure mentioned in section 4.4, where the MODIS 10-year averaged ε_s was used. The resultant LST are depicted in Figure 8.

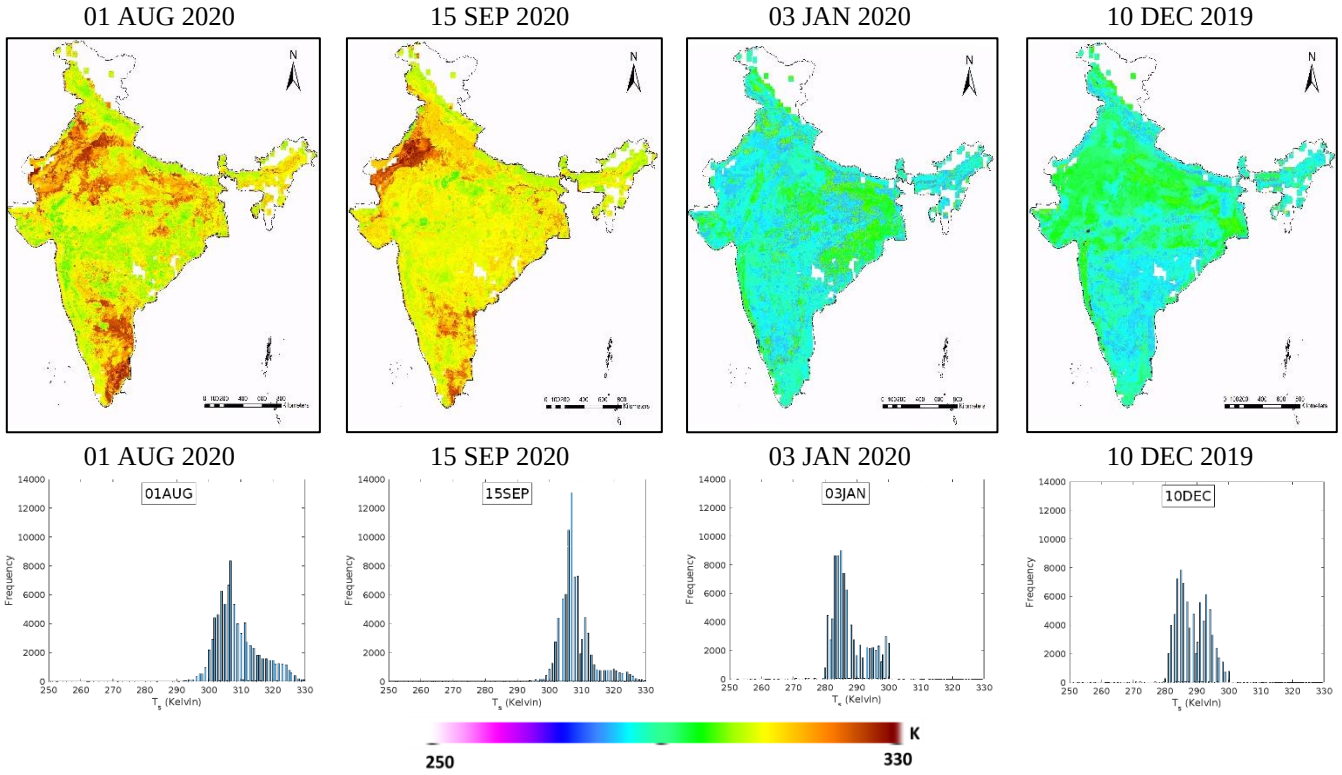

Figure 8. Model derived LST for selective dates over the span of 4 months in the years 2019-2020 at 0600 GMT and their respective histograms

The time scale shows the movement and transition between the different season, over the interval of 45 days between August-September and December-January. The histograms trends can depict the shift in temperature patterns with changing seasons. Higher T_s is noted in the north-western and south-eastern part, this is attributed due to the heavy influences of the agro-climatic regions of dry and desert [68]. This can be noted especially during the humid and overcast months of August and September. The 45-day interval also show the gradual shift within the environment with reduction in the maximum temperature, especially within the dry northwestern and southeastern regions due humidity. The months of January and December depicted a cooler environment, due to the winter period shadowed by fog presence. The histograms showed a strong concentration in the middle with a bi-peak for December in near symmetry due to the climatic variations between central and southern regions. This can be attributed primarily within the desert and humid regions within the area affected with fog presence [69].

The diurnal comparison of predicted T_s was made (Figure 9 and their statistics in Table 6) with T_s derived from measured longwave radiation flux components over different flux tower sites over five selected dates when surface radiation budget is generally strongly influenced by south-west and north-east monsoon clouds and fog.

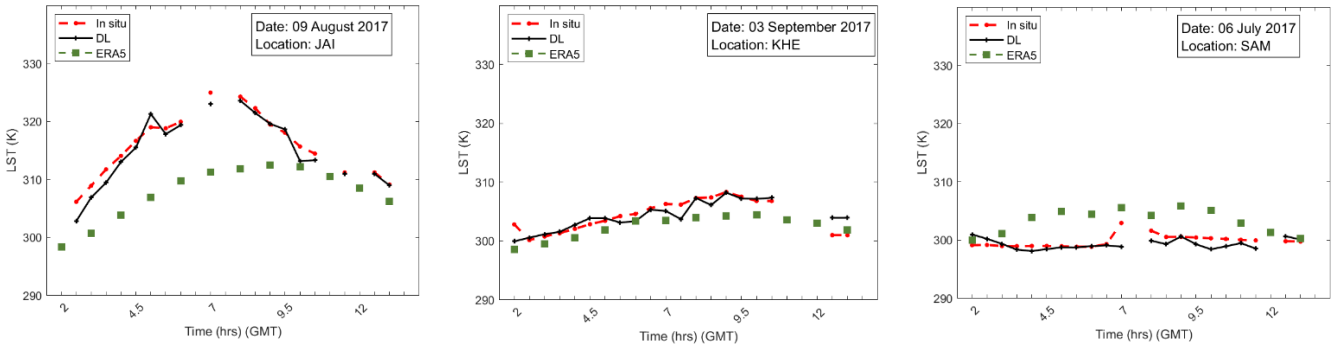

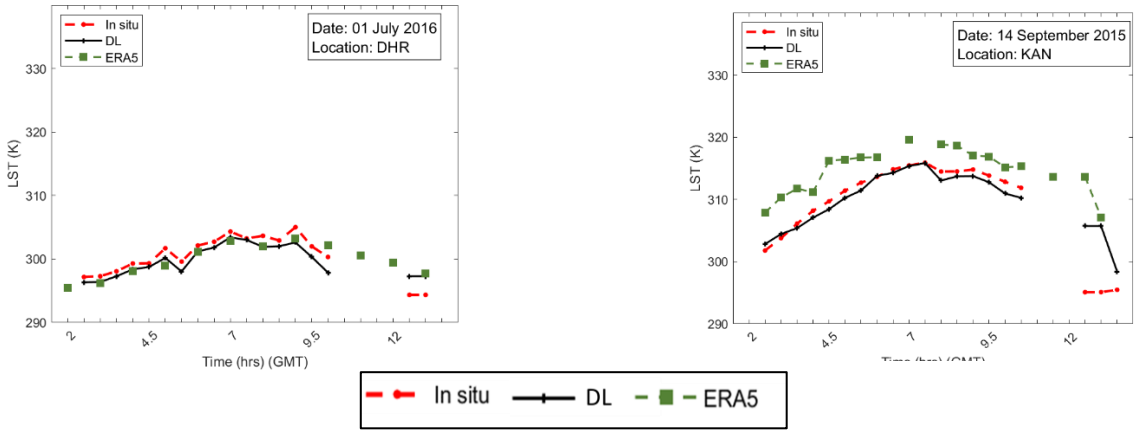

Figure 9. Diurnal Trends of LST over selective dates at different sites between spatial imagery derived from model, in situ and ERA5. The x-axis depicts time in GMT and y-axis depicts LST (in K).

Table 6. Variations in Ts between In-situ measurements, DL predicted and ERA5

Climate type	Flux tower sites	Daily mean T_s (K)			Difference in daily maximum T_s (K) w.r.t. measurements		Difference in daily minimum T_s (K) w.r.t. measurements	
		In situ measurements	DL-predicted	ERA5	DL-predicted	ERA5	DL-predicted	ERA5
Semi-arid	KHE	304.3	304.3	302.4	-0.1	-3.8	-0.2	-1.6
	DHR	300.4	299.7	299.8	-1.6	-1.8	2.0	1.1
Arid	JAI	315.9	315.0	307.7	-1.4	-12.5	-3.3	-7.8
Humid	SAM	299.8	299.3	303.3	-2.0	2.9	-0.7	1.1
	KAN	309.8	310.3	308.2	-0.1	-4.0	3.3	7.7

The diurnal trend over different times from the validation dataset are depicted. ERA5 reanalysis provide hourly T_s measurements, which were used as a comparative scale between the DL derived and in situ measurements. It can be seen, that DL and in situ measurements are closely matching with one another across all sites, with small exceptions due anomalies in specific periods. The trend was very well captured. The ERA5 provided higher values in regions like KAN and SAM, while lower in JAI. This is due to the agro-climatic zones where JAI is an arid region, while SAM and KAN are in a valley in the north mid-eastern part of India. The location and elevations are leading to more averaging and aggregated measurements over these specified sites. Whereas in regions with more uniform land use type like DHR and KHE, the ERA5, DL and in situ measurements were closely matching with one another. Further, a spatial difference between the DL and ERA5 measurements are depicted in Figure 10.

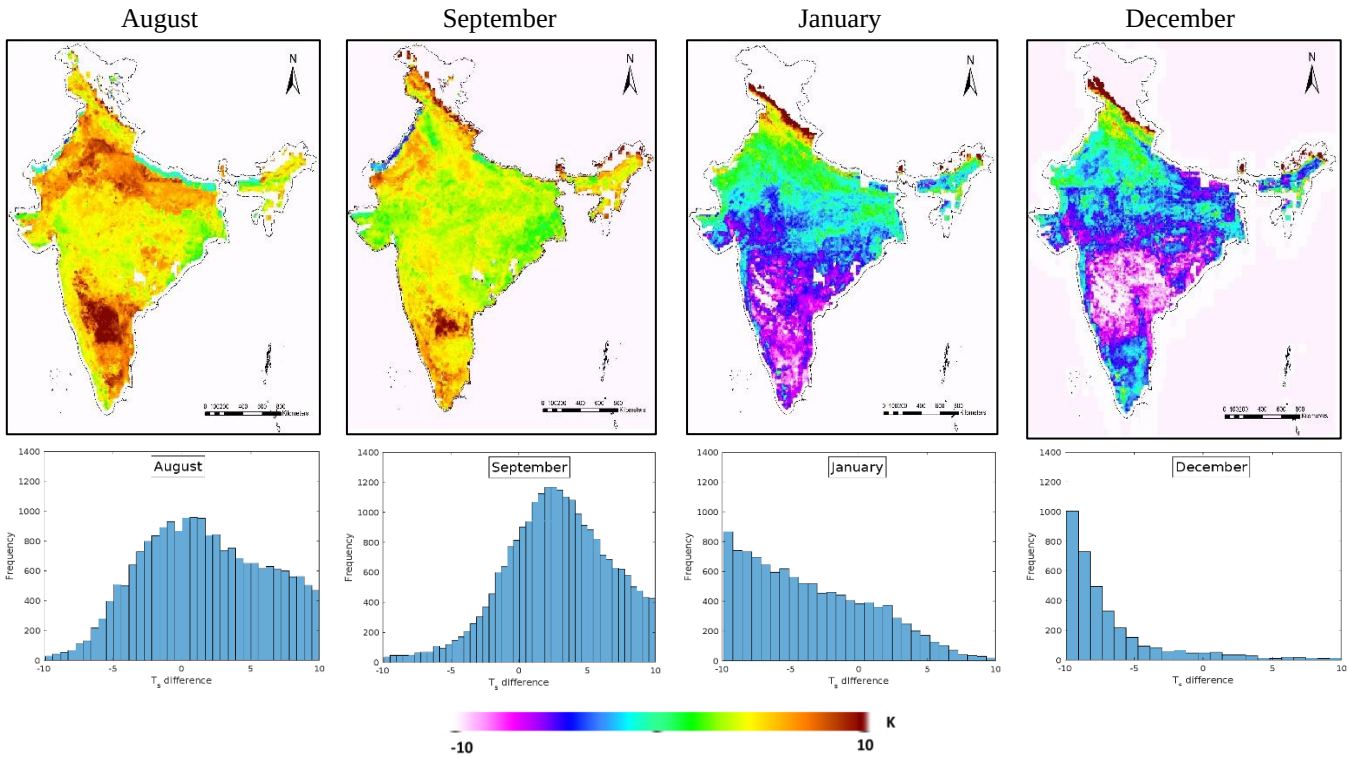

Figure 10. Difference between monthly averaged ERA5 Reanalysis and DL model derived LST for the year 2019-2020 at 0600 GMT and their respective histograms

The difference between the model and ERA5 reanalysis derived T_s depict an interesting pattern. Due to the process model derivation T_s, as well as aggregated upscaled 10km grid to match with the ERA5 spatial resolution, this has led to more undulations of T_s. The variations are ranging between -10 to 10 K. As it can be seen, the histogram spread for the same months have been shown.

The aggregation amounts of higher variations in regions where sudden changes in atmospheric and environmental conditions are evident. This is especially evident in the southern region of India, where higher positive difference was noted during the monsoon months of August and September, where high negative difference was noted during the winter months of December and January. The difference in between the two products is relatively close or near nil during the monsoon months of August and September. However, there is a systematic variation for the winter months of December. The attribution is also fueled with missing values within the region, especially in the Mid-Indian region. This is also leading to a skewness within the observations. While the DL derived T_S closely matches with the in-situ measurements, due to the spatial upscaling, similar to the NCEP product, higher difference is noted. Despite the same, the completed gap filled product is a new approach which can provide an alternative approach to retrieving T_s over the Indian landmass. The errors and variation can further be improved with higher-resolution products. The current model can be used to estimate operational regional-scale LW_{out} estimates after validation under overcast for some more months and over more in situ measurement sites. The generated LW_{out} can be used as an input for generation of T_s, which can be used to gap fill the current INSAT 3D T_s product.

Conclusion

A model investigating and retrieving LW_{out} and subsequently T_s was developed. The model was developed using in situ and satellite-based measurements. The study provided a first-hand understanding of the flow and behaviour of different fluxes and temperature over Indian landmass. The current model and methodology can be used to estimate LW_{out} and T_s over India only under cloudless conditions during daytime within 10% error overall.

Several uncertainties were identified during comparison with other established products. This was attributed to the scale-mismatch of inputs and measurements prints as well temporal scale differences. Despite the same, the diurnal trends show good agreement under different agroclimatic conditions over large temporal variations. The current model can be used to estimate operational regional-scale LW_{out} estimates after validation under overcast for some more months and over more in situ measurement sites. The generated LW_{out} can be used as an input for generation of T_s, which can be used to gap fill the current INSAT 3D T_s product.

Acknowledgement

The authors would like to thank SAC (Space Application Centre), ISRO, Ahmedabad and Dr. Bimal K Bhattacharya for providing datasets to carry out this study. The authors would like to specially thank Dr G S Bhat, PI INCOMPASS campaign, CAOS, IISc Bangalore and Dr R Morrison CEH, Wallingford, UK for providing the in-situ measurements relevant to this study.

Author Statement

Dhwanilnath Gharekhan conducted the validations, analysis, developed the model, and drafted as well as edited the manuscript.

References

[1] Z.-L. Li, B.-H. Tang, H. Wu, H. Ren, G. Yan, Z. Wan, I. F.Trigoe and J. A.Sobrinog, "Satellite-derived land surface temperature: Current status," *Remote Sensing of Environment,* vol. 131, pp. 14-37, 2013.

[2] A. J. Arnfield, ""Two decades of urban climate research: a review of turbulence, exchanges of energy and water, and the urban heat island," *International Journal of Climatology,* vol. 23, pp. 1-26, 2003.

[3] V. Lakshmi and D. Zehrfuhs, "Normalization and comparison of surface temperatures across a range of scales," *IEEE Transactions on Geoscience and Remote Sensing,* vol. 40, no. 12, pp. 2636 - 2646, 2002.

[4] B. Li, S. Liang, X. Liu, H. Ma, Yan, Chen, T. Liang and T. He, "Estimation of all-sky 1 km land surface temperature over the conterminous United States," *Remote Sensing of Environment,* vol. 266, p. 112707, 2021.

[5] A. Ohmura, "Physical basis for the temperature-based melt-index method," *Journal of Applied Meteorology,* vol. 40, no. 4, pp. 753 - 761, 2001.

[6] C. Wang, B.-H. Tang, H. Wu, R. Tang and Z.-L. Li, "Estimation of downwelling surface longwave radiation under heavy dust aerosol sky," *Remote Sensing,* vol. 9, no. 207, pp. 1 - 19, 2017.

[7] A. D. Culf and J. H. C. Gash, "Longwave radiation from clear skies in Niger: a comparison of observations with simple formulas," *Journal of Applied Meteorology,* vol. 32, no. 3, pp. 539 - 547, 1993.

[8] C.-H. Cheng and F. Nnadi, "Predicting Donward longwave radiation for various land use in all-sky conditions: Northeast florida," *Advances in Meteorology,* vol. 2014, pp. 1 - 12, 2014.

[9] R. G. Allen, L. S. Pereira, D. Raes and M. Smith, "Crop evapotranspiration - Guidelines for computing crop water requirements," *FAO - Food and Agriculture Organization of the United Nations,* pp. 1-15, 1998.

[10] J. Susskind, G. Molnar and L. Iredell, "Contributions to Climate Research Using the AIRS Science Team Version-5 Products," NASA, Houston, 2011.

[11] J. T. Liehl and E. K. Trenberth, “Earth's annual global mean energy budget,” *Bulletin fo American Meteorological Society 78 (2),* vol. 78, no. 2, pp. 197 - 208, 1997.

[12] M. Wild, M. Z. Hakuba, D. Folini1, P. Dörig-Ott, C. Schär and S. Kato, “The cloud-free global energy balance and inferred cloud radiative effects: an assessment based on direct observations and climate models,” *Climate Dynamics,* vol. 52, pp. 4787-4812, 2019.

[13] F. M. Pulselli and M. Maichi, “Global Warming Potential and the Net Carbon Balance,” *Encyclopedia of Ecology,* pp. 1741 - 1746, 2008.

[14] A. E. Dessler and M. D. Zelinka, “CLIMATE AND CLIMATE CHANGE | Climate Feedbacks,” in *Encyclopedia of Atmospheric Science,* G. R. North, J. Pyle and F. Zhang, Eds., Elsevier, 2015, pp. 18 - 25.

[15] M. Zhao, J.-C. Golaz, I. M. Held, V. Ramaswamy, S.-J. Lin, Y. Ming, P. Ginoux and B. Wyman, “Uncertainty in Model Climate Sensitivity Traced to Representations of Cumulus Precipitation Microphysics,” *Journal of Climate,* vol. 29, pp. 543-560, 2016.

[16] M. Wild, M. Z. Hakuba, D. Folini, P. Dörig-Ott, C. Schär, S. Kato and C. N. Long, “The cloud-free global energy balance and inferred cloud radiative effects: an assessment based on direct observations and climate models,” *Climate Dynamics* , vol. 52, pp. 4787 - 4812, 2019.

[17] S. Twomey, “Pollution and The Planetary Boundary,” *Atmopsheric Environment,* vol. 8, pp. 1251 - 56, 1974.

[18] G. Abramowitz, L. Pouyanne and H. Ajami, “On the information content of surface meteorology for downward atmospheric long-wave radiation synthesis,” *Geophysical research letters, Vol 39, Issue 4,* 2012.

[19] P. Gavilan, J. Berengena and R. Allen, “Measuring versus estimating net radiation and soil heat flux: impact on Penman-Monteith reference ET estimates in semiarid regions.,” *Agricultural Water Management,* vol. 89, no. 3, pp. 275 - 286, 2007.

[20] H. F. Duarte, N. L. Dias and S. R. Magiotto, “Assessing daytime downward longwave radiation estimates for clear and cloudy skies in souther Brazil,” *Agric, For. Meteorol. 139,* pp. 171 - 181, 2006.

[21] H. E. Snell, G. P. Anderson, J. L. M. J Wang, J. H. Chetwynd and S. J. English, “Validation of FASE (FASCODE for the Environment) and MODTRAN3: updates and comparison with clear-sky measurements,” *Proc. SPIE Int. Soc. Opt. Eng., 2578,* pp. 194 - 204, 1995.

[22] V. Elliott and S. R. L, “On the development of a simple downwelling longwave radiation scheme,” *Agric For. Meteorol, 112,* pp. 237 - 243, 2002.

[23] M. Choi, J. M. Jacobs and W. P. Kustas, “Assessment of clear and cloudy parameterization for daily downwelling longwave radiation over different land surfaces in Florida, USA,” *Geophysical Research Letters, 25,* 2008.

[24] K. Beven, “Towards integrated envrironmental models of everywhere: uncertainity, data and modelling as a learning process,” *Hydrol. Earth Syst. Sci.* , vol. 11, no. 1, pp. 460-467, 2007.

[25] P. C. Jain, “Greenhouse Effect and climate change: scientific basis and overview,” *Renewable Energy,* vol. 3, no. 4, pp. 403 - 420, 1993.

[26] A. Christen, F. Meier and D. Scherer, “High-frequency fluctuations of surface temperatures in an urban environment,” *Theoretical and Applied Climatology,* vol. 108, pp. 301-324, 2012.

[27] L. Spampinato, S. Calvari, C. Oppenheimer and E. Boschi, “Volcano surveillance using infrared cameras,” *Earth-Science Reviews,* vol. 106, no. 1-2, pp. 63-91, 2011.

[28] A. Laidi, R. Salah and H. Maamar, “An optimisation methodology of artificial neural network models for predicting solar radiation: a case study,” *Theor Appl Climatol,* 2015.

[29] A. G. Turner, G. S. Bhat, G. M. Martin, D. J. Parker, C. M. Taylor, A. K. Mitra, S. N. Tripathi, S. Milton, E. N. Rajagopal, J. G. Evans, R. Morrison, S. Pattnaik, M. Sekhar, B. K. Bhattacharya, R. Madan, M. Govindankutty, J. K. Fletcher and P. D. Wille, “Interaction of convective organization with monsoon precipitation, atmosphere, surface and sea: The 2016 INCOMPASS field campaign in India,” *Quaterly Journal of Royal Meteorological Society* , pp. 1-25, 2019.

[30] G. S. Bhat, R. Morrison, C. M. Taylor, B. K. Bhattacharya, S. Paleri1, D. Desai, J. G. Evans, S. Pattnaik, M. Sekhar, R. Nigam, A. Sattar, S. S. Angadi, D. Kacha11, A. Patidar, S. N. Tripathi, K. V. M. Krishnan and A. Sisodiya, “Spatial and temporal variability in energy and water vapour fluxes observed at seven sites on the Indian Subcontinent during 2017,” *Quarterly Journal of Royal Meteorological Society,* vol. 2, pp. 1 - 14, 2019.

[31] J. M. B. Jr., B. D. Tanner and B. Bugbee, “Evaluation of measurement accuracy and comparison of two new and three traditional net radiometers,” *Agriculture and Forest Meteorology,* vol. 149, no. 10, pp. 1709 - 1721, 2009.

[32] Kipps and Zonen, “CNR4 Net Radiometer,” 2019. [Online]. Available: https://www.kippzonen.com/Product/85/CNR4-Net-Radiometer.

[33] F. Rubel and M. Kottek, “Comments on: "The thermal zones of the Earth" by Wladimir Koppen (1884),” *Meteorological Zeitschrift,* vol. Vol 20, no. No 5, pp. 361 - 365, 2011.

[34] C. Wang, B. . Tang, H. Wu, R. Tang and Z. . Li, “ESTIMATION OF DOWNWELLING SURFACE LONGWAVE RADIATION UNDER THIN CIRRUS CLOUD SKY WITH ARTIFICIAL NEURAL NETWORK METHOD,” in *IGRASS,* 2017.

[35] F. Carmona, R. Rivas and V. Caselles, “Estimation of daytime download longwave radiation under clear and cloudy skies conditions over a sub-humid region,” *Theor. Appl. Climatol. 115,* pp. 281 - 295, 2014.

[36] J. Lhomme and L. Guiloni, “A simple model for minimum crop temperature forecasting during nocturnal cooling,” *Agriculture and Forest Meteorology 123,* pp. 55 - 68, 2004.

[37] C. Ruckstuhl, R. Philipona, J. Morland and A. Ohmura, “Observed relationship between surface specific humidity, integrated water vapor, and longwave downward radiation at different altitudes,” *Journal of Geophysical Research,* vol. 112, pp. D03302, 1- 7, 2007.

[38] M. Kanamitsu, W. Ebisuzaki, J. Woollen, S.-K. Yang, J. Hnilo, M. Fiorino and a. G. L. Potter, “NCEP-DOE AMIP-II Reanalysis (R-2),” *Bulletin of the American Meteorological Society. Nov,* pp. 1631 - 1643, 2002.

[39] J. J. Zyl, “The Shuttle Radar Topography Mission (SRTM): a breakthrough in remote sensing of topography,” *Acta Astronautica,* vol. 48, no. 5 - 12, pp. 559 - 565, 2001.

[40] F. Baret and M. Weiss, “ALGORITHM THEORETHICAL BASIS DOCUMENT [LEAF AREA INDEX (LAI) – VERSION 1, FRACTION OF ABSORBED PAR (FAPAR) – VERSION 1, FRACTION OF GREEN VEGETATION COVER (FCOVER)],” Copernicus , Netherlands, 2014.

[41] Copernicus, “Fraction of green Vegetation Cover,” 2014. [Online]. Available: https://land.copernicus.eu/global/products/fcover.

[42] D. Mankad, R. Sikhakolli, P. Kakkar, Q. Saquib, K. M. Agrawal, S. Gurjar, D. K. Jain, V. M. Ramanujam and P. Thapliyal, “SCATSAT-1 Scatterometer data processing,” *Current Science Special Section - SCATSAT 1,* vol. 117, no. 6, pp. 950-958, 2019.

[43] S. Singh, R. K. Tiwari, H. Gusain and V. Sood, “Potential Applications of SCATSAT-1 Satellite Sensor: A systematic review,” *EEE Sensors Journal,* pp. 1-13, 2020.

[44] M. Verma, J. B. Fisher, K. Mallick, Y. Ryu, H. Kobayashi, A. Guillaume, G. Moore, L. Ramakrishnan, V. Hendrix, S. Wolf, M. Sikka, G. Kiely, G. Wohlfahrt, B. Gielen, O. Roupsard and Piero, “Global Surface Net-Radiation at 5 km from MODIS Terra,” *Remote Sensing,* vol. 8, no. 739, pp. 1 - 20, 2016.

[45] H. Jiangtao, J. Gensuo, Z. Tianbao, W. Hesong and T. Bohui, “Satellite-Based Estimation of Daily Average Net Radiation Under Clear-Sky Conditions,” *Advances in Atmospheric Sciences,* vol. 31, pp. 705 - 720, 2014.

[46] B. K. Bhattacharya, C. Dutt and J. Parihar, “INSAT UPLINKED AGROMET STATION—A SCIENTIFIC TOOL WITH A NETWORK OF AUTOMATED MICROMETEOROLOGICAL MEASUREMENTS FOR SOIL-CANOPY-ATMOSPHERE FEEDBACK STUDIES,” *ISPRS Archives XXXVIII-8/W3 Workshop Proceedings: Impact of Climate Change on Agriculture ,* pp. 72 - 77, 2009.

[47] M. R. Pandya, D. B. Shah, H. J. Trivedi, S. Panigrahy, J. S. Parihar and A. S. Kirankumar, “Evaluation of split-window algorithms for retrieving land surface temperature from the INSAT-3D imager observations,” *Vayu Mandal,* vol. 37, no. 1 - 4, pp. 31 - 37, 2011.

[48] C. Cammalleri, M. C. Anderson, F. Gao, C. R. Hain and W. P. Kustas, “A data fusion approach for mapping daily evapotranspiration at field scale,” *Water Resources Research,* vol. 49, no. 8, pp. 4672-4686, 2013.

[49] D. V. Mahalakshmi, M. M. Ali, A. Pau, D. Dutta, J. R. Sharma, R. S. Reddy, C. Jha and V. K. Dadhwal, “Estimation of net surface radiation from eddy flux tower measurements using artifical neural network for cloudy skies,” *Sustainable Environmental Research 26,* pp. 44 - 50, 2016.

[50] P. Gupta and S. A. Christopher, “Particulate matter air quality assessment using integrated surface, satellite, and meteorological products: 2. A neural network approach,” *Journal of Geophysical Research: Atmosphere,* vol. 114, no. D20, p. D20205, 2009.

[51] A. S. Ahmadin, “Numerical Models for submerged breakwaters,” *Butterworth-Heinemann,* 2016.

[52] A. G. Ferreira, E. Soria-Olivas, A. J. S. López and E. Lopez-Baeza, “Estimating net radiation at surface using artificial neural networks: a new approach,” *Theor Appl Climatol 106,* pp. 263 - 279, 2011.

[53] N. Jankowski and W. Duch, “Optimal transfer function neural networks,” *ESANN'2001 proceedings - European Symposium on Artificial Neural Networks, Bruges (Belgium), 25-27 April,* pp. 101 - 106, 2001.

[54] P. Ramachandran, Q. B. Zoph and V. Le, “Searching for Activation Functions,” *arXiv,* p. 1710.05941, 2015.

[55] H. Takenaka, T. Y. Nakajima, A. Higurashi, A. Higuchi, T. Takamura, R. T. Pinker and a. T. Nakajima, "Estimation of solar radiation using a neural network based on radiative transfer," *Journal of Geophysical Research, Vol 116,* 2011.

[56] B. Jiang, Y. Zhang, S. Liang, X. Zhang and Z. Xiao, "Surface Daytime Net Radiation Estimation Using Artificial Neural Networks," *Remote Sensing,* pp. 11031-11050, 2014.

[57] D. V. Mahalakshmi, A. Paula, D. Dutta, M. M. Ali, C. S. Jha and V. K. Dadhwal, "NET SURFACE RADIATION RETRIEVAL USING EARTH OBSERVATION SATELLITE DATA AND MACHINE LEARNING ALGORITHM," in *ISPRS Annals of the Photogrammetry, Remote Sensing and Spatial Information Sciences, Volume II-8, 2014 ISPRS Technical Commission VIII Symposium,* Hyderabad, India, 2014.

[58] A. Velázquez-Blazquez, A. Geraldo-Ferreira, E. Soria-Olivas, J. Gómez-Sanchis, A. J. Serrano-López and E. López-Baeza, "Modelling net radiation at surface using ''in situ'' netpyrradiometer measurements with artificial neural networks," *Expert Systems with Applications,* vol. 38, pp. 14190 - 14195, 2011.

[59] A. Dolara, F. Grimaccia, S. Leva, M. Mussetta and E. Ogliari, "A Physical Hybrid Artificial Neural Network for Short Term Forecasting of PV Plant Power Output," *Energy,* vol. 8, pp. 1138 - 1153, 2015.

[60] J. Heaton, Introduction to Neural Networks with Java, Washington: Heaton Research Incorporated, 2008.

[61] R. Nigam, B. Bhattacharya, S. Vyas and M. Oza, "Retrieval of wheat leaf area index from AWiFS multispectral data using canopy radiative transfer simulation," *International Journal of Applied Earth Observation and Geoinformation,* vol. 32, no. Oct, pp. 173-185, 2014.

[62] D. Gharekhan, B. Bhattacharya, D. Desai and P. Patel, "Neural network-based approach for estimation of downwelling longwave radiation flux under cloudy-sky conditions," *Journal of Applied Remote Sensing,* vol. 15, no. 2, pp. 1-25, 2021.

[63] D. Gharekhan, B. K. Bhattacharya, D. Desai and P. R. Patel, "Modelling of downwelling longwave radiation over multiple agro-climate settings of India under foggy sky conditions–A neural network approach," *Remote Sensing Applications: Society and Environment,* vol. 25, p. 100684, 2022.

[64] NASA and S. Frazier, "MODIS Land Surface Temperature and Emissivity (MOD11)," 2019. [Online]. Available: https://modis.gsfc.nasa.gov/data/dataprod/mod11.php. [Accessed 10 Aug 2019].

[65] J. P. McCreary, W. Han, D. Shankar and S. R. Shetye, "Dynamics of the East India Coastal Current: 2. Numerical solutions," *JGR Oceans,* vol. 101, no. C6, pp. 13993 - 14010, 1996.

[66] F. Durand, D. Shankar, F. Bisol and S. S. C. Shenoi, "Spatiotemporal structure of the East India Coastal Current from satellite altimetry," *Journal of Geophysical Research,* vol. 114, no. C02013, pp. 1 - 18, 2009.

[67] S. Hellerman and M. Rosenstein, "Normal Monthly Wind Stress Over the World Ocean ith Error Estimates," *Journal of Phyiscal Oceanography,* vol. 13, pp. 1093 - 1104, 1983.

[68] A. Kar, B. K. Garg, M. P. Singh and S. Kathju, Trends in Arid Zone Research in India, Jodhpur: Central Arid Zone Research Institute, Jodhpur, 2009.

[69] C. Bharali, V. S. Nair, L. Chutia and S. S. Babu, "Modeling of the Effects of Wintertime Aerosols on Boundary Layer Properties Over the Indo Gangetic Plain," *Journal of Geophysical Research: Atmospheres,* vol. 124, no. 7, pp. 4141-4157, 2019.

[70] B. Backeberg, P. Penven and M. Rouault, “Impact of intensified Indian Ocean Winds on mesoscale variability in the Agulhas system,” *Nature climate change letters,* vol. 2, no. 8, pp. 608 - 612, 2012.

[71] S. Haykin, Neural networks: a comprehensive foundation, 2nd Edition, New Jersey: Prestine Hall, 1998.

[72] S. Bojinski, M. Verstraete, T. C. Peterson, C. Richter, A. Simmons and M. Zemp, “The concept of essential climate variables in support of climate research, application and policy,” *Americal Meteorological Society,* pp. 1431 - 1443, 2014.

[73] WMO, “The global observing system for climate: Implementation needs,” World Meteorological Organisation, Gauyaquil, Ecuador, 2016.

[74] T. Ming, R. De Richter, W. Liu and S. Caillol, “Fighting global warming by climate engineering: Is the earth radiation management and the solar radiation management any option for fighting climate change,” *Renewabale and Sustainable Energy Reviews, March, Vol 31,* pp. 792-834, 2014.

[75] B. Jianga, Y. Zhang, S. Lianga, G. Wohlfahrtc, A. Araind, A. Cescattie, T. Georgiadisf, K. Jiaa, G. Kielyg, M. Lundh, L. Montagnanii, V. M. j, P. S. Ortizl, W. Oechelm and F. P. Vac, “Empirical estimation of daytime net radiation from shortwave radiation and ancillary information,” *Agricultural and Forest Meteorology,* pp. 23-36, 2015.

[76] D. Male and R. Granger, “Snow surface energy exchange,” *Water Resource Res. 17 (3),* pp. 609 - 627, 1981.

[77] T. M. Crawford and C. E. Duchon, “An improved parameterization for estimating effective atmospheric emissivity for use in cacluating daytime longwave radiation,” *J. Appl. Meteorol. 38,* pp. 474-480, 1999.

[78] B. A. Forman and S. A. Margulis, “ High-resolution satellite-based cloud-coupled estimates of total downwelling surface radiation for hydrologic modelling applications,” *Hydrology and Earth System Sciences,* vol. 13, no. 7, pp. 969 - 986, 2009.

[79] B. H. Tang, Z.-L. Li and R. Zhang, “ A direct method for estimating net surface shortwave radiation from modis data,” *Remote Sensing of Environment,* vol. 103, no. 1, pp. 115 - 126, 2006.

[80] J. Kofronova, M. Tesar and V. Sipek, “The influence of observed and modelled net longwave radiation on the rate of estimated potential evapotranspiration,” *J. Hydrol. Hydromech.* , vol. 67, no. 3, pp. 280-288, 2019.

[81] J. T. Kiehl and K. E. Trenberth, “Earth’s Annual Global Mean Energy Budget,” *Bulletin of the American Meteorological Society,* vol. 78, no. 2, pp. 197-208, 1997.

[82] Z. Wei, X. Lee, X. Wen and W. Xiao, “Evapotranspiration partitioning for three agro-ecosystems with contrasting moisture conditions: a comparison of an isotope method and a two-source model calculation,” *Agriculture and Forest Meteorology,* vol. 252, pp. 296 - 310, 2018.

[83] S. Gupta, B. K. Bhattacharya and A. P. Krishnac, “A baseline regional evapotranspiration (ET) and change hotspots over Indian sub-tropics using satellite remote sensing data,” *Agricultural Water Management,* vol. 208, pp. 284 - 298, 2018.

[84] M. García, L. Villagarcía, S. Contreras, F. Domingo and J. Puigdefábregas, “Comparison of Three Operative Models for Estimating the Surface Water Deficit using ASTER Reflective and Thermal Data,” *Sensors,* vol. 7, pp. 860 - 883, 2007.